Published in final edited form as:
Eur J Nucl Med Mol Imaging. 2013 December ; 40(12): . doi:10.1007/s00259-013-2518-4.

The Complementary Roles of Dynamic Contrast Enhanced MRI and ^{18}F-Fluorodeoxyglucose PET/CT for Imaging of Carotid Atherosclerosis

Claudia Calcagno[1,2], **Sarayu Ramachandran**[1,2], **David Izquierdo-Garcia**[3], **Venkatesh Mani**[1,2], **Antoine Millon**[1,2], **David Rosenbaum**[4], **Ahmed Tawakol**[5], **Mark Woodward**[6], **Jan Bucerius**[7,8,9], **Erin Moshier**[10], **James Godbold**[10], **David Kallend**[11], **Michael E Farkouh**[12,13], **Valentin Fuster**[12,14], **James HF Rudd**[15], and **Zahi A Fayad**[1,2,12]

[1]Translational and Molecular Imaging Institute, Mount Sinai School of Medicine, New York, USA [2]Department of Radiology, Mount Sinai School of Medicine, New York, USA [3]Athinoula A. Martinos Center for Biomedical Imaging, Harvard University - MIT - Massachusetts General Hospital, Charlestown, MA, USA [4]Hopital Pitié Salpétrière, Paris, France [5]Harvard Medical School and Massachusetts General Hospital, Boston, Massachusetts, USA [6]George Institute, University of Sydney, Sydney, Australia [7]Department of Nuclear Medicine, Maastricht University Medical Center, Maastricht; the Netherlands [8]Cardiovascular Research Institute Maastricht (CARIM), Maastricht; the Netherlands [9]Department of Nuclear Medicine, Rheinisch-Westfaelische Technische Hochschule Aachen, Aachen; Germany [10]Biostatistics Shared Research Facility, Mount Sinai School of Medicine, New York, USA [11]F. Hoffmann-La Roche Ltd, Basel, Switzerland [12]Cardiovascular Institute, Mount Sinai School of Medicine, New York, USA [13]Peter Munk Cardiac Centre and Li Ka Shing Knowledge Institute, Toronto, Canada [14]The Centro Nacional de Investigaciones Cardiovasculares (CNIC), Madrid, Spain [15]Division of Cardiovascular Medicine, University of Cambridge, UK

Abstract

Background—Inflammation and neovascularization in vulnerable atherosclerotic plaques are key risk factors for severe clinical events. Dynamic contrast enhanced magnetic resonance imaging (DCE-MRI) and ^{18}F-fluorodeoxyglucose (FDG) positron emission tomography (PET) are two non-invasive imaging techniques capable of quantifying plaque neovascularization and inflammatory infiltrate respectively. However, their mutual role in defining plaque vulnerability and their possible overlap has not been thoroughly investigated. Here, we study the relationship between DCE-MRI and ^{18}F-FDG PET in the carotid arteries of 40 subjects with coronary heart disease (CHD) or CHD equivalent, recruited as a substudy of the dal-PLAQUE trial (NCT00655473).

Methods—The dal-PLAQUE trial was a multicenter study that evaluated dalcetrapib, a cholesteryl ester transfer protein modulator. Subjects underwent anatomical MRI, DCE-MRI and ^{18}F-FDG PET. Only baseline imaging and biomarkers data (before randomization) from dal-PLAQUE were used as part of this substudy. Our primary goal was to evaluate the relationship between DCE-MRI and ^{18}F-FDG PET data. As secondary endpoints, we evaluated the relationship between a) PET data and whole vessel anatomical MRI data, and b) DCE-MRI and matching anatomical MRI data. All correlations were estimated using a mixed linear model.

Corresponding author: Zahi A. Fayad, PhD Translational and Molecular Imaging Institute, Mount Sinai School of Medicine, One Gustave L. Levy Place, Box 1234 New York, NY 10029, USA Tel.: 1-212-241-6858 Fax: 1-212-534-2683 zahi.fayad@mssm.edu.

Results—We found a significant inverse relationship between several perfusion indices by DCE-MRI and ^{18}F-FDG uptake by PET. Regarding our secondary endpoints, there was a significant relationship between plaque burden measured by anatomical MRI with several perfusion indices by DCE-MRI and ^{18}F-FDG uptake by PET. No relationship was found between plaque composition by anatomical MRI with DCEMRI or ^{18}F-FDG PET metrics.

Conclusions—In this study we observed a significant, weak inverse relationship between inflammation measured as ^{18}F-FDG uptake by PET and plaque perfusion by DCE-MRI. Our findings suggest that there may be a complex relationship between plaque inflammation and microvascularization during the different stages of plaque development. ^{18}F-FDG PET and DCE-MRI may have complementary roles in identifying subjects at high risk for cardiovascular events in future clinical practice.

Keywords

DCE-MRI; PET/CT; atherosclerosis; inflammation; neovascularization

Introduction

In recent years, significant progress has been made in defining the hallmarks of high-risk, vulnerable atherosclerotic plaques. Vulnerable atheromas are characterized by a large lipid-rich necrotic core (LRNC), thin fibrous cap and prominent inflammatory infiltrate accompanied by abundant and fragile neovessels (1). This knowledge has stimulated the development of novel, non-invasive imaging techniques to identify vulnerable plaques, with the aim of improving risk stratification, follow-up and management of therapeutic intervention by directly preventing acute events (2). Techniques such as non-contrast-enhanced, anatomical magnetic resonance imaging (MRI), computed tomography (CT) and ultrasound can quantify anatomical characteristics and detect key components of vulnerable plaques. Other techniques can extract quantitative information about molecular mechanisms within the plaque. ^{18}F-fluorodeoxyglucose (FDG) positron emission tomography (PET) with CT and dynamic contrast-enhanced (DCE) MRI are measures of inflammation (3–5) and neovascularization (6–9) respectively, two features of plaque vulnerability. Both techniques show reasonable reproducibility (5,10) and have been used to track anti-atherosclerotic therapies in both clinical and pre-clinical trials (11–16). However, the possible degree of overlap of the information provided by each test has not been thoroughly investigated. In this study we investigated the relationship between ^{18}F-FDG PET/CT and DCE-MRI in the common carotid arteries of 40 subjects with either coronary heart disease (CHD) or CHD risk factors (CHD equivalent) recruited as part of the dal-PLAQUE multicenter trial (NCT00655473) (14,15).

Methods

Study Design

This study was conducted as part of the dal-PLAQUE multicenter trial that evaluated dalcetrapib, a cholesteryl ester transfer protein modulator (14,15). The protocol was reviewed and approved by the institutional review board of each participating center. Each participating center was trained in the image acquisition protocol by the core lab for image analysis of the dal-PLAQUE trial (Mount Sinai School of Medicine, New York, NY, USA). All participants provided written, informed consent. Here we report only baseline (prior to randomization) anatomical MRI, DCE-MRI, ^{18}F-FDG PET/CT and biomarkers data from the dal-PLAQUE study.

Study Population

The study population of dal-PLAQUE comprised patients with CHD or with CHD risk factors (CHD equivalent). Patients were clinically stable and receiving appropriate treatment with statin and/or other low-density lipoprotein cholesterol (LDL-C)-lowering drugs to achieve LDL-C levels of <100 mg/dL (<2.6 mmol/L), unless receiving maximum tolerated doses of therapy or intolerant to statins. Forty subjects were included in this study from the 189 screened in the dal-PLAQUE trial.

Image Acquisition

PET/CT—All PET scanners were fully calibrated and corrections applied for attenuation, isotope decay, dead time, normalization, sensitivity, scatter and random coincidences. Patients were instructed to avoid meals rich in carbohydrates starting from 12 hours before ^{18}F-FDG injection. Additionally subjects were asked to abstain from heavy physical activity for 24 hours before imaging to reduce muscle uptake of 18F-FDG. Approximately 30 minutes before 18FFDG injection, glucose was measured: if fasting blood glucose was higher than 200 mg/dL, imaging was rescheduled, otherwise patients were injected with15 mCi (555 MBq) ^{18}F-FDG, bought commercially from local vendors. After 120 min of FDG circulation time (3–5), a low dose, non-contrast-enhanced CT was performed for attenuation correction and anatomical co-registration. After aortic imaging for the purpose of the trials, carotid PET data were acquired in 3D-mode for 15 minutes, using 1 bed position, with the superior aspect of the field of view being the internal auditory meatus.

Anatomical MRI—Carotid MRI was performed on 1.5T clinical whole body systems (Siemens Medical Solutions, Erlangen, Germany) in the head-first supine position using a 4-channel carotid array (Machnet, Netherlands) for signal reception. Sixteen non-overlapping cross sectional T1 (echo time [TE], 9ms; repetition time [TR], 800ms), T2 (TE, 56ms; TR, 2000ms) and proton density (TE, 9ms; TR, 2000ms) weighted images were obtained using multi-slice, fat-saturated 2D turbo spin echo (TSE) acquisitions starting at, and extending below, the left carotid bifurcation as previously described (14,15). Dark blood was obtained using in-flow and out-flow saturation. Other relevant imaging parameters common to all three acquisitions were: field of view, 140×140 mm^2; matrix size, 256×256; in-plane spatial resolution, 0.55×0.55 mm^2; slice thickness, 3 mm; inter-slice gap, 0.3 mm; excitation flip angle, 90 degrees; refocusing angle, 180 degrees; turbo factor, 15; 4 signal averages.

DCE-MRI—DCE-MRI was performed on 1 selected axial slice (chosen from the T1-weighted image set, as the slice with the greatest degree of carotid wall thickening) using a black-blood, fat saturated TSE sequence after the injection of 0.2 mmol/kg gadolinium-diethylene triamine pentaacetic acid (Gd-DTPA, Magnevist, Bayer Schering Pharma) (6). Black blood was obtained using a double inversion recovery (DIR) technique. Relevant imaging parameters were: TE, 5.6 ms; TR, 250ms; field of view, 140×140 mm^2; matrix size, 256×256; in-plane spatial resolution, 0.55×0.55 mm^2; slice thickness, 3 mm; excitation flip angle, 90 degrees; refocusing angle, 180 degrees; turbo factor,15; 1 signal average; 100 measurements.

More details on PET and MRI acquisition parameters can be found in Fayad et al (14,15). For the purpose of this comparison, only data from 4 of the 11 imaging sites passed our imaging quality control, to ensure uniformity between MRI protocols, vendors and field strength.

Image Analysis

A schematic representation of the image analysis can be found in Figure 1.

Measurement of ^{18}F-FDG uptake—PET/CT images were analyzed using OsiriX (Geneva, Switzerland; http://www.osirix-viewer.com/) and in-house software for data handling. Arterial ^{18}F-FDG uptake was measured by drawing circular regions of interest (ROI) on all PET/CT slices of both common carotids. ROIs were fitted to the artery wall on each axial slice, while coronal and sagittal views were used to ensure that uptake was from the artery. Whole vessel mean, maximum and mean of maximum standardized uptake value (SUV) were recorded. Arterial SUV was normalized to blood pool SUV measured from 5 slices in the jugular vein, to calculate whole vessel mean, maximum and mean of maximum arterial target-to-background ratio (TBR) (5). SUV and TBR are both well-validated measures of ^{18}F-FDG uptake. To account for possible mis-registration errors between DCE-MRI and PET/CT data, we recorded mean, maximum and mean of maximum SUV and TBR across 5 slices centered on the slice matching with the DCE slice (Fig. 1, approximately 1 cm segment).

Anatomical MRI—Inner and outer vessel wall contours were manually traced by an experienced observer on all slices for both common carotids using T2-weighted multi-slice 2D-TSE images. Mean lumen diameter, vessel diameter, lumen area, wall area, total vessel area, mean wall thickness, standard deviation of wall thickness and normalized wall index for each slice were calculated using a customized software program (Vessel Mass Software, Leiden University Medical Center, The Netherlands) as previously described (17) and interfaced with in-house custom software for data analysis. Whole vessel parameters were recorded, as well as single slice values matched with DCE-MRI acquisition. Plaque component classification was performed by an experienced observer by looking simultaneously at the T1-, T2- and PD-weighted multi-slice 2D-TSE acquisitions to assess the presence or absence of LRNC, calcification and intra-plaque hemorrhage as described by Fayad et al (14,15). Plaque characterization was performed across the whole vessel as well as on the slice matching with the DCE-MRI acquisition.

DCE-MRI—The uptake of contrast agent was evaluated with a custom-made MATLAB (The MathWorks Inc., Natick, MA, USA) program (6). To ensure proper calibration between different imaging sessions, curves were converted to contrast agent concentration using the spoiled gradient echo signal model (18) and the widely-accepted linear relationship between relaxation rates and concentration. Contrast agent relaxivity was assumed to be 4.3 $mmol^{-1}s^{-1}$ (19). Kinetic modeling was performed using a population arterial input function (AIF) (20) and modified Tofts model (21). Kinetic parameters v_p (fraction of vascular space), K^{trans} (wash-in constant from plasma to tissue compartment), v_e (fraction of extra-vascular extracellular space), and K_{ep} (wash-out constant from tissue to plasma compartment) were calculated using standard non-linear least squares fittings (22) in Matlab. The non-model based parameter area under the concentration curve (AUC) (6,10–12) was also calculated at 1 (AUC1) and 2 minutes (AUC2) after injection of contrast agent (6) (Fig. 1).

Image co-registration between ^{18}F-FDG PET/CT and DCE-MRI—Anatomical co-registration between the DCE-MRI slice and the corresponding PET/CT slice was performed using automated registration of the CT- and PD-weighted high-resolution MR images using a Leonardo workstation (Siemens Medical Solutions, Erlangen, Germany). When necessary, manual adjustments were applied to correct for misalignments in the automated registration.

Statistical Methods

The main goal of our analysis was to correlate perfusion metrics by DCE-MRI with plaque inflammation as measured by ^{18}F-FDG PET/CT. We also assessed the correlation between: a) whole vessel PET/CT and whole vessel anatomical MRI variables and b) single-slice

perfusion measures by DCEMRI with matching single-slice anatomical MRI variables. Correlations were calculated using a mixed linear model with a compound symmetric correlation structure (23), implemented with PROC MIXED in SAS v. 9.2. All data were natural log-transformed to achieve Normality. This model accounts for the correlation between measurements of the same variable within each of the 40 patients in the study. The 95% confidence interval for each correlation coefficient was constructed using the bootstrap method (24), in which 1,000 bootstrap samples of size $n = 40$ were generated. Each sample consisted of 40 subjects being sampled with replacement from the complete list of 40 subjects; for each bootstrap sample, PROC MIXED calculated a correlation coefficient from the mixed model. The distribution of these 1,000 correlation coefficients provided estimates of the 2.5^{th} and the 97.5^{th} percentiles as the upper and lower confidence limits for the initial point estimate. When the 95% confidence interval did not include zero (limits had both the same sign, positive or negative) the correlation was considered significantly different from zero at the 5% level of significance. To adjust for the multiple statistical tests performed, Bonferroni correction was also applied to the comparisons presented in each table in the Results section. The p value of 0.05 used to establish significance was divided by the number of comparisons considered in each table (36 for Tables 2 and 5; 24 for Table 4). Therefore $p<0.001$ was required for the comparisons in Tables 2 and 5, and $p<0.02$ was required for the comparisons in Table 4 to reach statistical significance. The results are presented with and without Bonferroni correction. If correlation coefficients were less than 0.3, the correlation was considered weak; if higher or equal to 0.3 but lower than 0.7, the correlation was considered moderate; if higher or equal to 0.7, the correlation was considered to be strong.

Results

Patient Population

The mean age of the population was 64.2 years, and was mostly composed of males (78.8%). Baseline lipid biomarkers revealed average total cholesterol of 146.8 mg/dL, with average LDL-C being 74.8 mg/dL and high-density lipoprotein cholesterol being 45.8 mg/dL. Baseline demographics are reported in Table 1.

Relationship Between ^{18}F-FDG PET/CT and DCE-MRI

The relationship between DCE-MRI and PET variables was analyzed using a mixed linear model (Table 2). When comparing arterial FDG uptake by PET/CT and DCE-MRI measurements without Bonferroni correction, we found that the non-model-based parameter AUC1 showed a weak, significant inverse correlation with mean SUV, with correlation coefficient −0.23. The parameter AUC2 exhibited a weak, significant inverse correlation with maximum SUV (correlation coefficient −0.21). The model-based parameter K^{trans}, believed to represent a mixture of flow and permeability, exhibited a weak, significant inverse correlation with maximum SUV (correlation coefficient −0.22), mean TBR (correlation coefficient −0.24; Fig. 2A) and mean of maximum TBR (correlation coefficient −0.22). The model based parameter v_p, expressing the fractional plasma volume, showed a moderate, inverse significant correlations with the mean SUV calculated (correlation coefficient −0.41) and the mean of maximum SUV (correlation coefficient −0.32). The model based parameter K_{ep} (backflow constant from tissue to plasma) showed weak, inverse significant correlations with mean SUV and TBR (correlation coefficients −0.28 and −0.23; Fig. 2B) and mean of maximum SUV and TBR (correlation coefficients −0.24 and −0.20). Model-based parameter v_e did not show any significant correlation with SUV and TBR values. No significant correlations were found when using Bonferroni correction. Figure 3 shows PET/CT images and DCE-MRI uptake curves from 2 patients representative of our sample. In the upper part of the figure, a patient presenting with low ^{18}F-FDG uptake by

PET/CT but high Gd-DTPA uptake by DCE-MRI is displayed (A–C). Conversely, in the lower part of the figure, a patient presenting with high ^{18}F-FDG and low Gd-DTPA uptake is shown (D–F).

Correlation between Anatomical MRI and PET/CT

Table 3 shows the results of analysis of whole-vessel anatomical MRI data. The dataset is composed mainly of non-complex carotid atherosclerotic plaques, with calcification being identified in only 15.1% and LRNC in 36.4% of the lesions. Intra-plaque hemorrhage was absent from the entire cohort of subjects in this substudy. Among the slices chosen for DCE-MRI, 6.1% showed calcification and 18.2% revealed an LRNC. Mean wall thickness averaged across the whole vessel calculated from anatomical MRI data showed moderate but significant positive correlations with the average whole vessel TBR, with correlation coefficient 0.39 (Table 4) without Bonferroni correction. No significant correlations were found between any of the PET variables and plaque composition by MRI (data not shown). No significant correlations were found when using Bonferroni correction.

Correlation between Anatomical MRI and DCE-MRI

Analysis of high-resolution anatomical MRI data revealed weak, positive significant correlation of average and standard deviation of wall thickness with the DCE-MRI parameter K_{ep} (correlation coefficients 0.21 and 0.25 respectively) when not using Bonferroni correction. No significant correlation was found between DCE-MRI metrics and plaque composition by MRI (data not shown). No significant correlations were found when using Bonferroni correction.

Discussion

The main goal of this study was to investigate the relationship between ^{18}F-FDG PET/CT and DCE-MRI in the carotid arteries of 40 patients with CHD or CHD risk equivalent recruited as part of the dal-PLAQUE study (14,15). These techniques offer a quantitative read-out for plaque macrophages (4) and neovessels respectively (6,7), two of the hallmarks of plaque vulnerability. We found a significant weak inverse relationship between the two techniques. As secondary endpoints, we explored the relationships between non-contrast-enhanced anatomical MRI and both DCE-MRI and FDG PET/CT. Anatomical MRI showed a significant weak positive correlation with DCE-MRI and a significant weak inverse correlation with PET/CT.

Previous studies have investigated the relationship between anatomical MRI and ^{18}F-FDG PET/CT and found higher FDG uptake in complex lesions, but no or only weak correlation with plaque wall thickness. Silvera et al found higher FDG uptake in lipid-based compared to collagen-rich or calcified plaques using TBR (25). Additionally (only in the LRNC group), they found a significant TBR variation according to the median of the vessel wall thickness. On the contrary, Kwee et al (26) found higher FDG uptake measured as SUV in fibrous, but not lipid-rich, plaques. Additionally, they found a correlation between SUV and vessel wall volume. Here, we confirm a significant relationship between average whole vessel TBR by PET/CT and average wall thickness by anatomical MRI, but fail to demonstrate a correlation between FDG uptake and plaque composition (Table 4). This difference from the two aforementioned studies may be due to the patient population and nature of the lesions (more complex in other studies, versus non-complex in the present study). Additionally we demonstrate weak but significant correlation between anatomical MRI measures such as average wall area and average and standard deviation of wall thickness and the DCE-MRI metric K_{ep}, while no correlation was found with plaque composition (Table 5).

Recently, Cyran et al (27) have studied the relationship between ^{18}F-FDG PET/CT and DCE-MRI in patients with supra-aortic arteritis, and found a positive significant correlation between mean arterial TBR and extraction fraction of MRI contrast agent. Taqueti et al (28) also found a positive significant correlation between FDG uptake measured as TBR and K^{trans} by DCE-MRI and neovessels by histology in patients with severe carotid stenosis. Here we demonstrate a weak but significant inverse correlation between model- and non-model based DCE-MRI metrics and SUV and TBR by PET/CT. This difference in findings may be due to several reasons. Firstly, it must be noted that the patient populations in the two studies are very different: while Taqueti et al (28) studied subjects presenting with a high degree of carotid stenosis, in this study we investigated subjects with non-complex atherosclerotic lesions (Table 3). Differences in medication usage between the population investigated in this study and other studies may also act as confounding factors. Additionally, while it is known that PET/CT and DCE-MRI provide a read-out for plaque macrophages and neovessels, their metrics may not exclusively reflect such histological features. For example, contrast agent extravasation in DCE-MRI depends not only on neovessel density and permeability, but also on the fractional extra-vascular extra-cellular space available for contrast agent distribution (21). Alternatively, it is possible that plaque macrophage content and neovascularization (and therefore ^{18}F-FDG PET and DCE-MRI) may exhibit different relationships with each other depending on the stage of the plaque that is being imaged.

Another potential explanation for our findings resides in the interplay between neovascularization, hypoxia and inflammation (29). It is relatively well established that hypoxia and inflammation are intertwined at the molecular, cellular and clinical levels (30). Hypoxic conditions are known to develop in atherosclerotic plaques as a result of smooth muscle cell proliferation in the tunica intima, subsequent wall thickening and increased oxygen consumption by macrophages and foam cells (31–33). Hypoxia induces increased glycolysis (34,35) in macrophages (hence increased FDG uptake). In addition to increasing macrophage glycolysis, hypoxia is known to increase macrophage activation, phagocytosis (36) and tumor necrosis factor production (37). This hypothesis offers a possible explanation for our findings, where higher FDG uptake was inversely correlated with plaque neovascularization by DCE-MRI. It is therefore possible to envision a scenario where the hypoxia-driven inflammatory response may precede an increase in plaque neovascularization by neoangiogenesis (38). This hypothesis has been corroborated by more recent *in vivo* findings by Pedersen et al (39), which described the relationship between SUV and expression of genes of plaque vulnerability and neoangiogenesis in human carotid specimens. This study found a significant but negative correlation between CD34, a histological marker of micro-vessel density, and both SUV by ^{18}F-FDG-PET and CD68, a histological marker of macrophages. No correlation was found between SUV and markers of neoangiogenesis (vascular endothelial growth factor). The authors concluded that ^{18}F-FDG uptake inversely reflects micro-vessel density, but not neoangionegesis in human atherosclerotic plaques. Since DCE-MRI metrics are known to reflect plaque neovessels content, this may explain the higher substantial ^{18}F-FDG uptake in areas of low uptake of Gd-DTPA by DCE-MRI and vice versa.

Together with other studies, our findings suggest that ^{18}F-FDG PET and DCE-MRI may offer complementary, non-overlapping information about vascular inflammation and neoangiogenesis. This suggests that these two techniques may be used in combination in future clinical practice for accurate staging and risk stratification of atherosclerotic plaques. However, a more thorough investigation of these two modalities and their underlying histological correlates at the different stages of plaque progression is needed before their translation into clinical care.

Study Limitations

Possible limitations of the study are as follows. Firstly, the sample size was relatively small (40 subjects) and comparison of the imaging findings with a histological gold standard was not possible. Due to small sample size, subgroup analyses of symptomatic versus asymptomatic subjects were also not possible. Secondly, DCE-MRI achieved limited single slice coverage to maintain sufficiently fast temporal resolution (4.8 s) together with high-spatial resolution (0.5mm × 0.5mm) for the reliable estimation of contrast agent uptake and good characterization of plaque composition. This required careful matching of DCE-MRI slices with the corresponding anatomical MRI and PET/CT images, which may be affected by mis-registration. The development of novel technologies such as integrated PET/MRI scanners will, in the future, allow these studies to be performed simultaneously, naturally providing co-registered PET and MRI images and therefore eliminating this issue (40). PET imaging has quite poor spatial resolution to image small structures, such as the atherosclerotic vessel wall. However, this modality has been used successfully in combination with CT, which provides anatomical details and attenuation correction, to quantify inflammation in atherosclerotic plaques (4). Novel PET/MRI may allow the application of partial volume correction techniques, to help image small structures, such as the vasculature, with increased accuracy (41). A black-blood sequence was chosen for DCE-MRI acquisition, to allow better delineation of these non-complex atherosclerotic lesions from the vessel lumen during dynamic scans. Despite allowing for clear visualization of the arterial vessel wall by suppressing the blood signal, black-blood imaging does not allow for sampling a per-patient AIF for kinetic modeling. A population derived AIF (20) was used for analysis, which may introduce inaccuracies in the calculation of model-based parameters. Finally, no significant correlations were found when using Bonferroni correction. While Bonferroni correction is applied when multiple statistical tests are performed to avoid type 1 errors (false positives), it is a rather conservative approach which does increase the chance of type 2 errors (false negatives). While some of the correlations reported without Bonferroni correction are likely to be false positives, in this case the correction demands $p<0.001$ (Tables 2 and 5) and $p<0.002$ (Table 4) to reach significance. As this may conceivably have led to some false negatives, both corrected and uncorrected results were reported.

In conclusion, in this study we find a significant inverse relationship between non-model and model-based perfusion indices by DCE-MRI (indices of neovascularization) and SUV and TBR by PET/CT (markers of macrophage content). This finding, in combination with other findings in the literature, suggests that there may be a complex relationship between plaque inflammation and neovascularization, and that ^{18}F-FDG PET and DCE-MRI images have complex histological correlates, whose relationship may change during the different stages of plaque progression. The combination of PET-CT and DCE-MRI imaging may prove to be a useful tool in drug development for proof of concept of new therapies.

Supplementary Material

Refer to Web version on PubMed Central for supplementary material.

Acknowledgments

F. Hoffmann-La Roche Ltd funded the dal-PLAQUE study and provided third-party editorial support, through Prime Healthcare Ltd, for the preparation of the manuscript. CC has received grant or research support from the National Institutes of Health and National Heart Lung and Blood Institute (NIH/NHLBI R01 HL071021, NIH/NHLBI R01 HL078667 and NIH/NCRR UL1RR029887). SR, DI-G, AM, DR, JB, EM, JG and VF indicate that they have nothing to disclose. VM discloses that he receives consulting fees from Tursiop Inc. AT discloses that he has received honoraria from Roche, BMS and Novartis, and research grants from Merck, BMS, Genentech, GSK and VBL. MW discloses that he has received honoraria from Roche. DK is an employee of F. Hoffmann-La Roche

Ltd. MEF discloses that he has received honoraria from Roche and acted as a consultant to Genentech. JHFR. discloses that he has received honoraria from Roche and is part-supported by the National Institute for Health Research Cambridge Biomedical Research Centre. ZAF discloses that he has received research grants from Roche, GlaxoSmithKline, Merck, VBL Therapeutics, Novartis, Bristol-Myers Squibb, and Via Pharmaceuticals, and honoraria from Roche.

References

1. Virmani R, Burke AP, Farb A, Kolodgie FD. Pathology of the vulnerable plaque. J Am Coll Cardiol. 2006; 47(suppl):C13–C18. [PubMed: 16631505]
2. Fuster V, Fayad ZA, Moreno PR, Poon M, Corti R, Badimon JJ. Atherothrombosis and high-risk plaque: Part II: approaches by noninvasive computed tomographic/magnetic resonance imaging. J Am Coll Cardiol. 2005; 46:1209–1218. [PubMed: 16198833]
3. Rudd JH, Warburton EA, Fryer TD, et al. Imaging atherosclerotic plaque inflammation with [18F]-fluorodeoxyglucose positron emission tomography. Circulation. 2002; 105:2708–2711. [PubMed: 12057982]
4. Tawakol A, Migrino RQ, Bashian GG, et al. In vivo 18F-fluorodeoxyglucose positron emission tomography imaging provides a noninvasive measure of carotid plaque inflammation in patients. J Am Coll Cardiol. 2006; 48:1818–1824. [PubMed: 17084256]
5. Rudd JH, Myers KS, Bansilal S, et al. (18)Fluorodeoxyglucose positron emission tomography imaging of atherosclerotic plaque inflammation is highly reproducible: implications for atherosclerosis therapy trials. J Am Coll Cardiol. 2007; 50:892–896. [PubMed: 17719477]
6. Calcagno C, Cornily JC, Hyafil F, et al. Detection of neovessels in atherosclerotic plaques of rabbits using dynamic contrast enhanced MRI and 18F-FDG PET. Arterioscler Thromb Vasc Biol. 2008; 28:1311–1317. [PubMed: 18467641]
7. Kerwin W, Hooker A, Spilker M, et al. Quantitative magnetic resonance imaging analysis of neovasculature volume in carotid atherosclerotic plaque. Circulation. 2003; 107:851–856. [PubMed: 12591755]
8. Kerwin WS, O'Brien KD, Ferguson MS, Polissar N, Hatsukami TS, Yuan C. Inflammation in carotid atherosclerotic plaque: a dynamic contrast-enhanced MR imaging study. Radiology. 2006; 241:459–468. [PubMed: 16966482]
9. Kerwin WS, Oikawa M, Yuan C, Jarvik GP, Hatsukami TS. MR imaging of adventitial vasa vasorum in carotid atherosclerosis. Magn Reson Med. 2008; 59:507–514. [PubMed: 18306402]
10. Calcagno C, Vucic E, Mani V, Goldschlager G, Fayad ZA. Reproducibility of black blood dynamic contrast-enhanced magnetic resonance imaging in aortic plaques of atherosclerotic rabbits. J Magn Reson Imaging. 2010; 32:191–198. [PubMed: 20578026]
11. Lobatto ME, Fayad ZA, Silvera S, et al. Multimodal clinical imaging to longitudinally assess a nanomedical anti-inflammatory treatment in experimental atherosclerosis. Mol Pharm. 2010; 7:2020–2029. [PubMed: 21028895]
12. Vucic E, Dickson SD, Calcagno C, et al. Pioglitazone modulates vascular inflammation in atherosclerotic rabbits noninvasive assessment with FDG-PET-CT and dynamic contrast-enhanced MR imaging. JACC Cardiovasc Imaging. 2011; 4:1100–1109. [PubMed: 21999870]
13. Vucic E, Calcagno C, Dickson SD, et al. Regression of inflammation in atherosclerosis by the LXR agonist R211945: a noninvasive assessment and comparison with atorvastatin. JACC: Cardiovascular Imaging. 2012; 5:819–828. [PubMed: 22897996]
14. Fayad ZA, Mani V, Woodward M, et al. Rationale and design of dal-PLAQUE: a study assessing efficacy and safety of dalcetrapib on progression or regression of atherosclerosis using magnetic resonance imaging and 18F-fluorodeoxyglucose positron emission tomography/computed tomography. Am Heart J. 2011; 162:214–221. [PubMed: 21835280]
15. Fayad ZA, Mani V, Woodward M, et al. Safety and efficacy of dalcetrapib on atherosclerotic disease using novel non-invasive multimodality imaging (dal-PLAQUE): a randomised clinical trial. Lancet. 2011; 378:1547–1559. [PubMed: 21908036]
16. Fayad ZA, Mani V, Fuster V. The time has come for clinical cardiovascular trials with plaque characterization as an endpoint. Eur Heart J. 2012; 33:160–161. [PubMed: 21875863]

17. Mani V, Muntner P, Gidding SS, et al. Cardiovascular magnetic resonance parameters of atherosclerotic plaque burden improve discrimination of prior major adverse cardiovascular events. J Cardiovasc Magn Reson. 2009; 11:10. [PubMed: 19393089]
18. Haacke, EM.; Brown, RW.; Thompson, MR.; Venkatesan, R. Magnetic Resonance Imaging, Physical Principles and Sequence Design. J Wiley & Sons; New York, NY: 1999.
19. Sasaki M, Shibata E, Kanbara Y, Ehara S. Enhancement effects and relaxivities of gadolinium-DTPA at 1.5 versus 3 Tesla: a phantom study. Magn Reson Med Sci. 2005; 4:145–149. [PubMed: 16462135]
20. Parker GJ, Roberts C, Macdonald A, et al. Experimentally-derived functional form for a population-averaged high-temporal-resolution arterial input function for dynamic contrast-enhanced MRI. Magn Reson Med. 2006; 56:993–1000. [PubMed: 17036301]
21. Tofts PS, Brix G, Buckley DL, et al. Estimating kinetic parameters from dynamic contrast-enhanced T(1)-weighted MRI of a diffusable tracer: standardized quantities and symbols. J Magn Reson Imaging. 1999; 10:223–232. [PubMed: 10508281]
22. Murase K. Efficient method for calculating kinetic parameters using T1-weighted dynamic contrast-enhanced magnetic resonance imaging. Magn Reson Med. 2004; 51:858–862. [PubMed: 15065262]
23. Hamlett A, Ryan L, Wolfinger R. On the use of PROC MIXED to Estimate Correlation in the Presence of Repeated Measures. SAS Users' Group International, Proceedings of the Staqtistics and Data Analysis Section. 2004:1–7. paper 198-29.
24. Efron, B.; Tibshirani, RJ. An Introduction to the Bootstrap. Chapman & Hall; New York, NY: 1993.
25. Silvera SS, Aidi HE, Rudd JH, et al. Multimodality imaging of atherosclerotic plaque activity and composition using FDG-PET/CT and MRI in carotid and femoral arteries. Atherosclerosis. 2009; 207:139–143. [PubMed: 19467659]
26. Kwee RM, Teule GJ, van Oostenbrugge RJ, et al. Multimodality imaging of carotid artery plaques: 18F-fluoro-2-deoxyglucose positron emission tomography, computed tomography, and magnetic resonance imaging. Stroke. 2009; 40:3718–3724. [PubMed: 19875738]
27. Cyran CC, Sourbron S, Bochmann K, et al. Quantification of supra-aortic arterial wall inflammation in patients with arteritis using high resolution dynamic contrast-enhanced magnetic resonance imaging: initial results in correlation to [18F]-FDG PET/CT. Invest Radiol. 2011; 46:594–599. [PubMed: 21577125]
28. Taqueti V, Carli MD, Jerosch-Herold M, et al. Increased microvascular blood flow and permeability associates with FDG signal in human atheroma. J Am Coll Cardiol. 2012; 59(suppl):E1309.
29. Minchenko A, Leshchinsky I, Opentanova I, et al. Hypoxia-inducible factor-1-mediated expression of the 6-phosphofructo-2-kinase/fructose-2,6-bisphosphatase-3 (PFKFB3) gene. Its possible role in the Warburg effect. J Biol Chem. 2002; 277:6183–6187. [PubMed: 11744734]
30. Eltzschig HK, Carmeliet P. Hypoxia and inflammation. N Engl J Med. 2011; 364:656–665. [PubMed: 21323543]
31. Moreno PR, Purushothaman KR, Fuster V, et al. Plaque neovascularization is increased in ruptured atherosclerotic lesions of human aorta: implications for plaque vulnerability. Circulation. 2004; 110:2032–2038. [PubMed: 15451780]
32. Fuster V, Moreno PR, Fayad ZA, Corti R, Badimon JJ. Atherothrombosis and high-risk plaque: part I: evolving concepts. J Am Coll Cardiol. 2005; 46:937–954. [PubMed: 16168274]
33. Ribatti D, Levi-Schaffer F, Kovanen PT. Inflammatory angiogenesis in atherogenesis--a double-edged sword. Ann Med. 2008; 40:606–621. [PubMed: 18608127]
34. Folco EJ, Sheikine Y, Rocha VZ, et al. Hypoxia but not inflammation augments glucose uptake in human macrophages: Implications for imaging atherosclerosis with 18fluorine-labeled 2-deoxy-D-glucose positron emission tomography. J Am Coll Cardiol. 2011; 58:603–614. [PubMed: 21798423]
35. Kawaguchi T, Veech RL, Uyeda K. Regulation of energy metabolism in macrophages during hypoxia. Roles of fructose 2,6-bisphosphate and ribose 1,5-bisphosphate. J Biol Chem. 2001; 276:28554–28561. [PubMed: 11373280]

36. Anand RJ, Gribar SC, Li J, et al. Hypoxia causes an increase in phagocytosis by macrophages in a HIF-1alpha-dependent manner. J Leukoc Biol. 2007; 82:1257–1265. [PubMed: 17675562]

37. Leeper-Woodford SK, Detmer K. Acute hypoxia increases alveolar macrophage tumor necrosis factor activity and alters NF-kappaB expression. Am J Physiol. 1999; 276:L909–916. [PubMed: 10362714]

38. Moulton KS. Angiogenesis in atherosclerosis: gathering evidence beyond speculation. Curr Opin Lipidol. 2006; 17:548–555. [PubMed: 16960504]

39. Pedersen SF, Graebe M, Hag AM, Hoejgaard L, Sillesen H, Kjaer A. Microvessel density but not neoangiogenesis is associated with 18F-FDG uptake in human atherosclerotic carotid plaques. Mol Imaging Biol. 2012; 14:384–392. [PubMed: 21732164]

40. Yankeelov TE, Peterson TE, Abramson RG, et al. Simultaneous PET-MRI in oncology: a solution looking for a problem? Magn Reson Imaging. 2012; 30:1342–1356. [PubMed: 22795930]

41. Torigian DA, Zaidi H, Kwee TC, Saboury B, Udupa JK, Cho ZH, Alavi A. PET/MR imaging: technical aspects and potential clinical applications. Radiology. 2013; 267:26–44. [PubMed: 23525716]

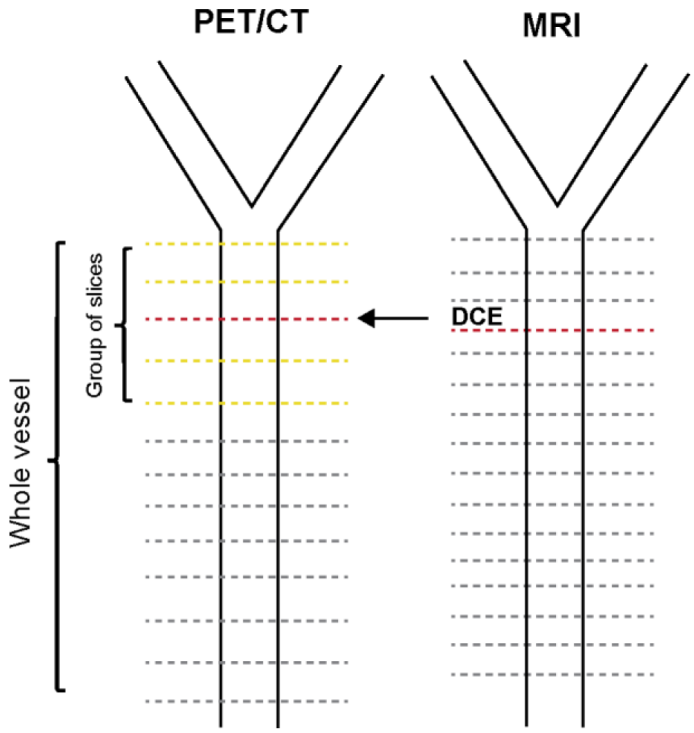

FIGURE 1.
Schematic view of image analysis in common carotid arteries. Dashed lines represent acquired PET/CT and MRI axial slices. Data from all the slices was used for the whole vessel analyses. Red dashed line, DCE-MRI slice. Orange dashed lines, PET slices surrounding the slice matched with DCE-MRI, included in the analysis to take into account possible mis-registrations between the two techniques.
PET/CT = positron emission tomography/computer tomography; MRI = magnetic resonance imaging; DCE = dynamic contrast enhanced MRI

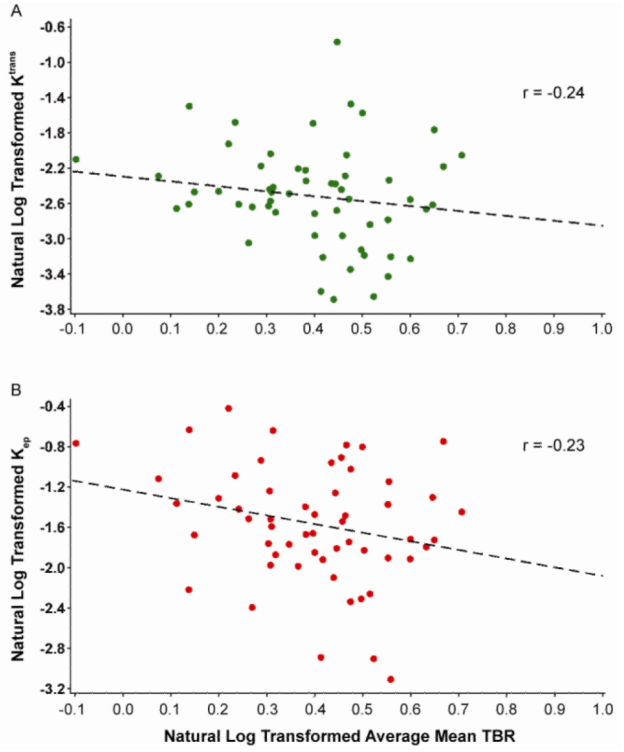

FIGURE 2.

Correlation between DCE-MRI and mean TBR by PET/CT, in the carotid arteries of subjects with CHD or CHD risk equivalent. (A) Correlation between K^{trans} by DCE-MRI and mean TBR by PET/CT. (B) Correlation between K_{ep} by DCE-MRI and mean TBR by PET/CT. x axis, mean TBR; y axis, DCE-MRI variables. Black dotted line, regression line. K^{trans} = wash-in constant from plasma to tissue constant; K_{ep} = wash-out constant from tissue to plasma; TBR = target-to-background ratio.

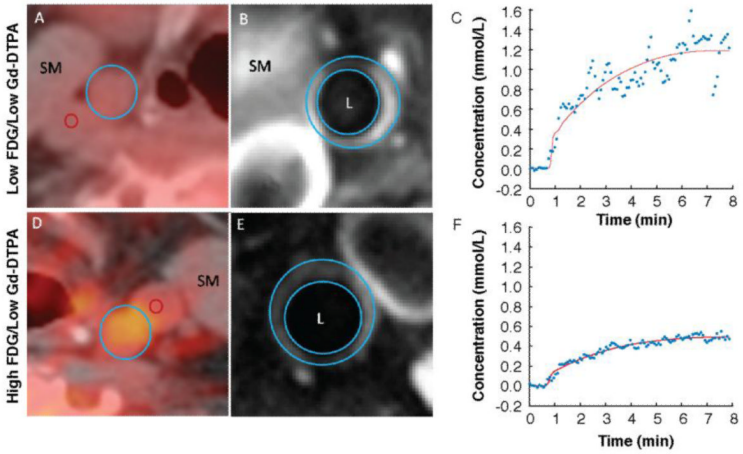

FIGURE 3.

Sample patient DCE-MRI and ^{18}F-FDG PET/CT images showing the relationship between Gd-DPTA uptake and ^{18}F-FDG uptake. (A–C) representative case with low arterial FDG uptake by PET/CT, but high Gd-DTPA uptake by DCE-MRI. (D–F) representative case with high arterial FDG uptake by PET/CT, but low Gd-DTPA uptake by DCE-MRI. (A) and (D) FDG PET image overlaid on CT image.; blue circle, common carotid artery; red circle, jugular vein. (B) and (E) T1W post-contrast MRI image. (C) and (F) kinetic modeling of Gd-DTPA uptake by DCE-MRI. X-axis, time (min); y-axis, concentration (mmol/L); blue dots, experimental data; red line, model fit.

FDG = fluorodeoxyglucose; Gd-DTPA = gadolinium-diethylene triamine pentaacetic acid; SM = skeletal muscle; L = vessel lumen.

TABLE 1

Baseline patient characteristics

Characteristic	n =33
Mean age, y (SD)	64 (8.0)
Male sex, n (%)	26 (78.8)
Body mass index, kg/m^2 (SD)	29 (5.1)
Medical history, n (%)	
Type II diabetes	10 (30.3)
Hypertension	20 (60.6)
CHD	28 (84.8)
Abdominal aortic aneurysm	1 (3.0)
Symptomatic carotid disease	3 (9.1)
Peripheral arterial disease	2 (6.1)
Smoking	4 (12.1)
Lipids (mg/dL)	
Total cholesterol	146.8 (29.0)
LDL-C	74.8 (19.8)
HDL-C	45.8 (14.7)
Triglycerides (mg/dL)	130.7 (64.1)
hsCRP (mg/dL)	2.6 (3.5)

Data are mean (SD) unless otherwise stated

SD = standard deviation; CHD = coronary heart disease; LDL-C = low-density lipoprotein-cholesterol; HDL-C = high-density lipoprotein-cholesterol; hsCRP = high-sensitivity C-reactive protein.

TABLE 2

Correlation between DCE-MRI and slice-matched ^{18}F-FDG PET/CT

	PET/CT parameters					
DCE-MRI parameters	**AUC1**	**AUC2**	**K^{trans}**	**v_e**	**K_{ep}**	**v_p**
SUV_Mean	**− 0.23**	−0.22	−0.25	0.02	**− 0.28**	**− 0.41**
SUV_Max	−0.18	**− 0.21**	**− 0.22**	−0.04	−0.20	−0.25
SUV_MeanofMax	−0.20	−0.20	−0.22	0.02	**− 0.24**	**− 0.32**
TBR_Mean	−0.23	−0.20	**− 0.24**	−0.02	**− 0.23**	−0.30
TBR_Max	−0.10	−0.11	−0.15	−0.14	−0.04	−0.29
TBR_MeanofMax	−0.20	−0.19	**− 0.22**	−0.04	**− 0.20**	−0.29

$n = 40$. Bold red values indicate significant correlations without Bonferroni correction ($P < 0.05$).

PET = positron emission tomography; CT = computer tomography; DCE-MRI = dynamic contrast enhanced magnetic resonance imaging; AUC = area under the curve; K^{trans} = wash-in constant from plasma to tissue constant; V_e = fraction of extravascular extracellular space; K_{ep} = wash-out constant from tissue to plasma; V_p = fraction of vascular space; SUV = standardized uptake value; TBR = target-to-background ratio.

TABLE 3

Non-contrast-enhanced MRI analysis

Measure (mean and standard deviation)	Whole vessel (n =33)	DCE-MRI slice (n = 40)
Average total vessel area (cm^2)	0.61 (0.20)	0.60 (0.13)
Average wall area (cm^2)	0.28 (0.11)	0.24 (0.06)
Average lumen area (cm^2)	0.32 (0.11)	0.36 (0.08)
Average mean wall thickness (mm)	1.15 (0.24)	0.97 (0.20)
Average standard deviation of wall thickness (mm)	0.27 (0.19)	0.20 (0.11)
Average normalized wall index (a.u.)†	0.46 (0.07)	0.40 (0.06)
Calcification (n, %)	5 (15.1)	2 (6.1)
Hemorrhage (n,%)	0 (0)	0 (0)
Lipid rich necrotic core (n, %)	12 (36.4)	6 (18.2)

†Average normalized wall index was the wall area/total vessel area ratio based on the average of the right and left carotids.

DCE-MRI = dynamic contrast enhanced magnetic resonance imaging; a.u. absolute units.

TABLE 4

Correlation between anatomical MRI and whole-vessel PET/CT

	Average SUV	Maximum SUV	Average TBR	Maximum TBR
Average total vessel area (cm^2)	0.04	0.00	0.12	0.08
Average wall area (cm^2)	0.05	0.00	0.29	0.23
Average lumen area (cm^2)	0.03	0.01	−0.09	−0.10
Average mean wall thickness (mm)	0.05	0.01	**0.39**	0.33
Average standard deviation of wall thickness (mm)	0.01	−0.03	0.30	0.24
Average normalized wall index (a.u.)	0.04	0.01	0.33	0.29

Bold red values indicate significant correlations without Bonferroni correction ($P < 0.05$).

SUV = standardized uptake value; TBR = target-to-background ratio; a.u. absolute units.

TABLE 5

Correlation between anatomical MRI and DCE-MRI

	AUC1	AUC2	K^{trans}	v_e	K_{ep}	v_p
Average total vessel area (cm^2)	0.10	0.11	0.09	0.06	0.06	0.12
Average wall area (cm^2)	0.14	0.17	0.15	0.00	0.16	0.09
Average lumen area (cm^2)	0.08	0.07	0.04	0.09	−0.02	0.10
Average mean wall thickness (mm)	0.11	0.14	0.16	−0.05	**0.21**	0.07
Average standard deviation of wall thickness (mm)	0.08	0.08	0.07	−0.21	**0.25**	−0.16
Average normalized wall index (a.u.)	0.07	0.10	0.15	−0.11	0.24	0.00

Bold red values indicate significant correlations without Bonferroni correction ($P < 0.05$).

AUC = area under the curve; K^{trans} = wash-in constant from plasma to tissue constant; V_e = fraction of extravascular extracellular space; K_{ep} = wash-out constant from tissue to plasma; V_p = fraction of vascular space; a.u. absolute units.